Journal of Materials Science: Materials in Electronics (2019) 30:5681–5690
https://doi.org/10.1007/s10854-019-00861-9

Fabrication of CdS quantum dot/Bi_2S_3 nanocomposite photocatalysts for enhanced H_2 production under simulated solar light

S. V. Prabhakar Vattikuti[1] · P. C. Nagajyothi[1] · Jaesool Shim[1]

Received: 5 December 2018 / Accepted: 29 January 2019 / Published online: 14 February 2019

Abstract
CdS quantum dots (CdSQDs) contain unique structural features and are an attractive class of visible-light-driven photocatalysts that have been used as catalyst supports. In this study, ethylene glycol assisted synthesis of CdSQD nanobunches are successfully self-assembled with Bi_2S_3 nanorods via a simple hydrothermal method and are applied as a photocatalyst for H_2 production. Because of the unique nanostructure, the CdSQDs/Bi_2S_3 composite achieved a 24.9-fold higher yield than that of pristine Bi_2S_3. In addition, the CdSQDs/Bi_2S_3 composite could be recovered and reused without the loss of its catalytic activity for three cycling tests. Coupling the CdSQDs with Bi_2S_3 nanorods with tight contacts could improve the development of profiled binary composites for various applications.

1 Introduction

Because of the global energy consumption and demand, numerous studies have evaluated alternative energy source materials [1]. Hydrogen is an alternative source to transitional fossil fuels [2, 3]. Photocatalytic hydrogen production has received interest and concern owing to the use of solar energy. Conventional TiO_2 has been investigated as a photocatalyst for solar energy conversion [4]. However, it is more active under ultraviolet (UV) irradiation, which hinders the transition from research to practical applications. Therefore, several strategies have been adapted to develop visible-light-driven photocatalytic materials for the efficient utilization of sun light [5, 6]. Among the various visible-light-driven photocatalysts, cadmium sulfide (CdS) with a band gap from 2.55 to 2.8 eV is regarded as the best candidate for various photocatalytic applications owing to its favorable band position and its visible light absorption capability [7, 8]. For the effective utilization of solar light, CdS should be developed as an efficient visible-light-driven photocatalytic material. However, CdS has demonstrated lower photocatalytic efficiency and lower long-term stability [9]. Therefore, numerous studies have been performed, including the coupling of semiconductors to form a heterostructure, surface deposition of a noble metal, and doping of transition metals have recently received huge attention from materials scientists due to their unique structural benefits. One strategy includes the development of heterostructure semiconductors as a visible-light-driven photocatalytic material, combining two or more semiconductors to form a composite with high active sites and advanced structural features [9, 10].

Among the various semiconductor materials, Bi_2S_3 has proven to be a remarkable photocatalyst for the degradation of pollutants and hydrogen production [11, 12]. Bi_2S_3 is a narrow band gap semiconductor. Recently, different combinations of Bi_2S_3 based composites, such as C@Bi_2S_3 [13], Bi_2WO_6/Bi_2S_3 [14], Bi_2S_3/BiOCl [15], Bi_2S_3/$SnIn_4S_8$ [16], Bi_2S_3/Bi_2WO_6 [17], and Bi_2S_3/RGO [18], were stated to be latent materials because of their high photocatalytic activity. Recently, a Bi_2S_3/ZnS nanoplate composite with a high photodegradation efficiency of 87.7% gained immense attention as it demonstrated remarkable photocatalytic properties for the degradation of a methylene blue (MB) pollutant [19]. In addition, Bi_2S_3 also accelerated the photoreaction progress by generating more superoxide radicals [20]. Wang et al. synthesized a heterojunction consisting of $Bi_2O_2CO_3$ nanoparticles on Bi_2S_3 that demonstrated a high photocatalytic activity for the degradation of rhodamine-B (RhB) dye [21]. Chachvalvutikul et al. successfully synthesized $ZnIn_2S_4$/Bi_2S_3 that showed a higher photocatalytic activity than that

✉ S. V. Prabhakar Vattikuti
vsvprabu@gmail.com

✉ Jaesool Shim
jshim@ynu.ac.kr

[1] School of Mechanical Engineering, Yeungnam University, 214-1 Dae-dong Gyeongsan-si, Gyeongsan, Gyeongsangbuk-do 712-749, South Korea

of pristine Bi_2S_3 [22]. In other report, Li et al. reported biomolecule assisted synthesized CdS and Bi_2S_3 nanomaterials with Pt supported catalyst demonstrated excellent photocatalytic hydrogen production [23]. However, these noble metal supported composites are more expensive, limited to use.

In our previous study, the C@Bi_2S_3 heterojunction demonstrated a high photocatalytic hydrogen evolution rate under visible light [13]. All of these successful examples show that Bi_2S_3-based composite photocatalysts are potential photocatalysts because of their remarkable photocatalytic properties. To develop CdSQDs as an efficient visible-light-driven photocatalyst, the CdSQDs could be coupled with the Bi_2S_3 materials to form a heterostructure that could be applied as a photocatalytic for photocatalytic hydrogen production. Hao et al. [24] reported that the Bi_2S_3/CdS heterojunction demonstrated a 5.5 mmol $h^{-1}g^{-1}$ hydrogen production rate under visible light irradiation. Li et al. [25] used Bi_2S_3/CdS photocatalysts for photoreduction of CO_2 into methanol under visible light irradiation.

Based on these existing reports, nanobunches of CdS quantum dots (CdSQDs) anchored on Bi_2S_3 nanorods were synthesized to improve the photocatalytic hydrogen evolution of Bi_2S_3 nanorods under simulated solar light irradiation. The CdSQDs/Bi_2S_3 composite was successfully prepared by simple mixing of pure components without using surfactants. The specific surface area of the Bi_2S_3 nanorods was increased with the introduction of the CdSQDs, which enhanced the photocatalytic hydrogen evolution. Because of the unique structure, the CdSQDs/Bi_2S_3 composite demonstrated a 41.67 mmol $g^{-1}h^{-1}$ hydrogen evolution rate after 5 h of simulated solar light irradiation. The visible-light-driven photocatalytic hydrogen production mechanism is subsequently described.

2 Experimental details

All reagents were received and used as provided without further processing.

2.1 Synthesis of the Bi_2S_3 nanorods

The Bi_2S_3 nanorods were produced via a hydrothermal method. The synthetic process involved adding Bi (NO_3) (3.4 mmol) and CH_4N_2S (16.5 mmol) to 70 mL of ethylenediamine. After stirring for 1 h, the solution was transformed to a Teflon-lined autoclave and was maintained at 200 °C for 4 h. After completion of the reaction, the products were collected using a centrifuge at 5000 rpm and washed several times with deionized water and ethanol to remove any impurities. Finally, the products were dried at 110 °C for 5 h to obtain the final products.

2.2 Synthesis of the CdSQD nanobunches

Ethylene glycol (EG) was used as a stabilizer for the synthesis of the CdS nanobunches. In a typical synthesis, 0.76 g of Cd $(NO_3)_2{\cdot}4H_2O$ is dissolved in ethanol and stirred for 10 min under an ambient temperature. Then, 71.8 mM of thioacetamide (C_2H_4NS) in 7.5 mL of ethanol is added quickly to the above solution under stirring. Then, $NH_3{\cdot}H_2O$ (2 mL) and ethylene glycol (2.5 mL) is added. The resultant solution is transferred to a Teflon sealed autoclave and maintained at 200 °C for 5 h. After cooling to room temperature, the yellow products are collected by a centrifuge at 5000 rpm, washed with DI water and ethanol several times, and dried in a vacuum oven at 110 °C for 5 h.

2.3 Synthesis of the CdSQDs/Bi_2S_3 nanocomposite

To synthesize the CdSQDs/Bi_2S_3 nanocomposite, 2 g of Bi_2S_3 was dissolved in 50 mL of *N,N*-dimethylformamide under ultra-sonication, followed by stirring for 1 h. After stirring for 1 h, 1 g of CdSQD powder was poured into the above dispersion, and the mixture was subjected to an ultrasonic treatment for 2 h followed by 3 h of stirring to obtain close interfacial contact between CdS and the Bi_2S_3 nanorods. The final products were collected by a centrifuge at 5000 rpm, washed several times with ethanol to remove the impurities, and heated in a vacuum oven at 100 °C for 12 h to achieve the final composite.

2.4 Characterization

The morphologies of the samples were measured using a scanning electron microscope (SEM, S-4100 model) and a high-resolution transmission electron microscope (HRTEM) with an accelerating voltage of 110 KV. An X-ray diffraction technique and X-ray photoelectron spectroscopy (XPS, Thermo scientific k-alpha surface analyzer) were used to test the structural purity of the samples. The optical absorption measurements were conducted using (Cary 5000) a UV–Vis spectrophotometer. The N_2-adsorption–desorption isotherms were measured using a Micromeritics ASAP 2420 surface area analyzer. Before gas adsorption, the samples were degassed at 180 °C for 1 h. The functional groups were tested using Fourier transform infrared (FTIR) spectrometry (PerkinElmer, USA), ranging from 400 to 4000 cm^{-1}.

2.5 Photocatalytic hydrogen production

The photocatalytic H_2 tests were performed in a 150-mL quartz reactor at room temperature and atmospheric pressure. The opening of the flask was sealed with a silicone

rubber spectrum. The photocatalysts (5 mg) were dispersed in an aqueous solution (50 mL) containing 0.25 mol L^{-1} of Na_2SO_3 and Na_2S as electron donors. A 300-W (MaX 303 model) Xe lamp was used as a solar light source. The output of the light intensity was fixed to 50 mW cm^{-2}. Before irradiation, the reactor system was evacuation by a vacuum pump and bubbled with N_2 for 20 min to remove the air inside the reactor. The produced hydrogen gas was measured using an off-line gas chromatograph (GC, YL-6500 instrument) equipped with a thermal conductivity detector and a 5-A molecular sieve column. Here, 250 µL of produced hydrogen gas in the head space of the system was collected and injected manually into the GC and estimated by a calibration plot to 5% standard hydrogen gas. The carrier gas in the GC system was He.

2.6 Photoelectrochemical tests

The photocurrent was measured, and electron impedance spectroscopy (EIS) was performed using a three-electrode cell, where Ag/AgCl was employed as the reference electrode and a platinum coil was used as the counter electrode at an ambient temperature. An indium tin oxide (ITO) glass substrate was used as the working electrode. The preparation method of the working electrode was as follows: 10 mg of the sample was mixed with 450 µL of DI water and 50 µL of Nafion, creating a slurry, which was applied on the ITO glass substrate by a drop casting method. Then, the working electrode was heated to 80 °C for 1 h. The photocurrent measurements were conducted with a 300-W Xe lamp. EIS was performed over a frequency of 100 mHz to 1 MHz at the open circuit with an alternative current potential amplitude of 2 mV. All the electrochemical experiments were performed on a SP-200 Bio-logic workstation.

3 Results and discussion

Figure 1 shows the XRD pattern of the pristine Bi_2S_3, CdSQDs, and CdSQDs/Bi_2S_3 nanocomposite. The XRD pattern of the prepared Bi_2S_3 showed the formation of an orthorhombic structure of Bi_2S_3 with broad reflection peaks ascribed to fine particle nanostructures, corresponding to JCPDS No 86-8964 [26]. While, the CdSQD XRD pattern showed distinct peaks at (111), (200), (221), and (311) were indexed to the cubic phase (JCPDS no 75-1545) and hexagonal phase (JCPDS no 10-0453) structures with broadening peaks owing to the reduction of the crystallite size. The prominent peak at 26.8° matched well with the cubic phase, and the other peaks matched the hexagonal phase. Similar results have been reported for the cubic and hexagonal phases of CdS [27, 28]. Based on the Scherer formula for (111) [29], the crystallite size of the CdSQDs

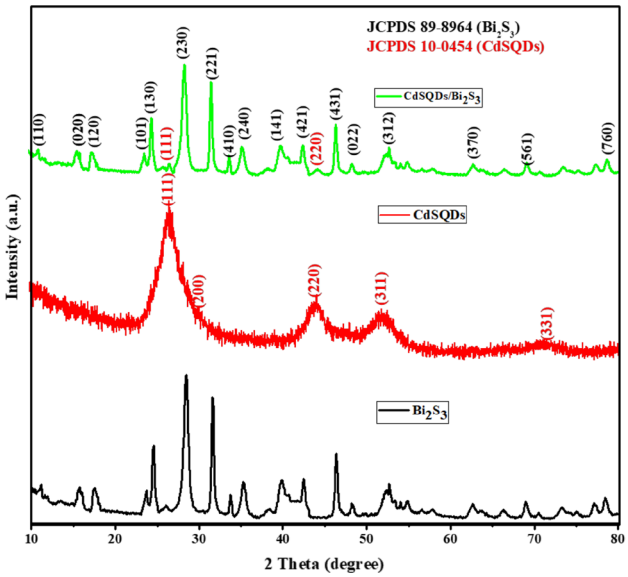

Fig. 1 XRD pattern of pristine Bi_2S_3, CdSQDs, and CdSQDs/Bi_2S_3 nanocomposite

was approximately 4.5 nm. For the CdSQDs/Bi_2S_3 nanocomposite, a coexisting phase of CdS and Bi_2S_3 materials was confirmed. The XRD pattern results of the CdSQDs/Bi_2S_3 nanocomposite showed that the CdSQDs had successfully deposited on the surface of the Bi_2S_3 nanorods.

The morphological properties of the photocatalysts were characterized by SEM, TEM, and HRTEM. Figure 2a, b shows the SEM images of the CdSQDs/Bi_2S_3 heterojunction without the addition of surfactants. Bunches of CdSQDs were tightly attached to the surface or side of the Bi_2S_3 nanorods, forming nanocomposites. The SEM images of the CdSQDs/Bi_2S_3 Fig. 2c–f shows representative Bi_2S_3 nanorods with a diameter of approximately 70 nm and a uniform rod like (1D) morphology anchored by a number of CdSQDs. These QDs were 5–6 nm in size. While, the CdSQDs consisted of bunches of quantum dots stacked together. In addition, the HRTEM results also confirmed the formation of the heterojunction of the CdSQDs/Bi_2S_3 composite, as shown in Fig. 2c–f. As shown by HRTEM (Fig. 2f), clear lattice fringes with interplanar spacings of 0.33 nm and 0.36 nm could be indexed to the (002) plane of the CdS cubic phase and the (310) plane of the Bi_2S_3 orthorhombic phase, respectively, suggesting that the synthesized catalyst demonstrated good crystallinity [30]. The results showed the formation of heterojunctions by the coupling of the CdSQDs with the Bi_2S_3 nanorods. Figure 3 shows the SEM EDX spectra of CdSQDs/Bi_2S_3 nanocomposite, which confirmed the formation of heterostructure contains no trace of impurities.

Figure 4 shows the XPS elemental composition and chemical status of the CdSQDs/Bi_2S_3 nanocomposite. Figure 4a

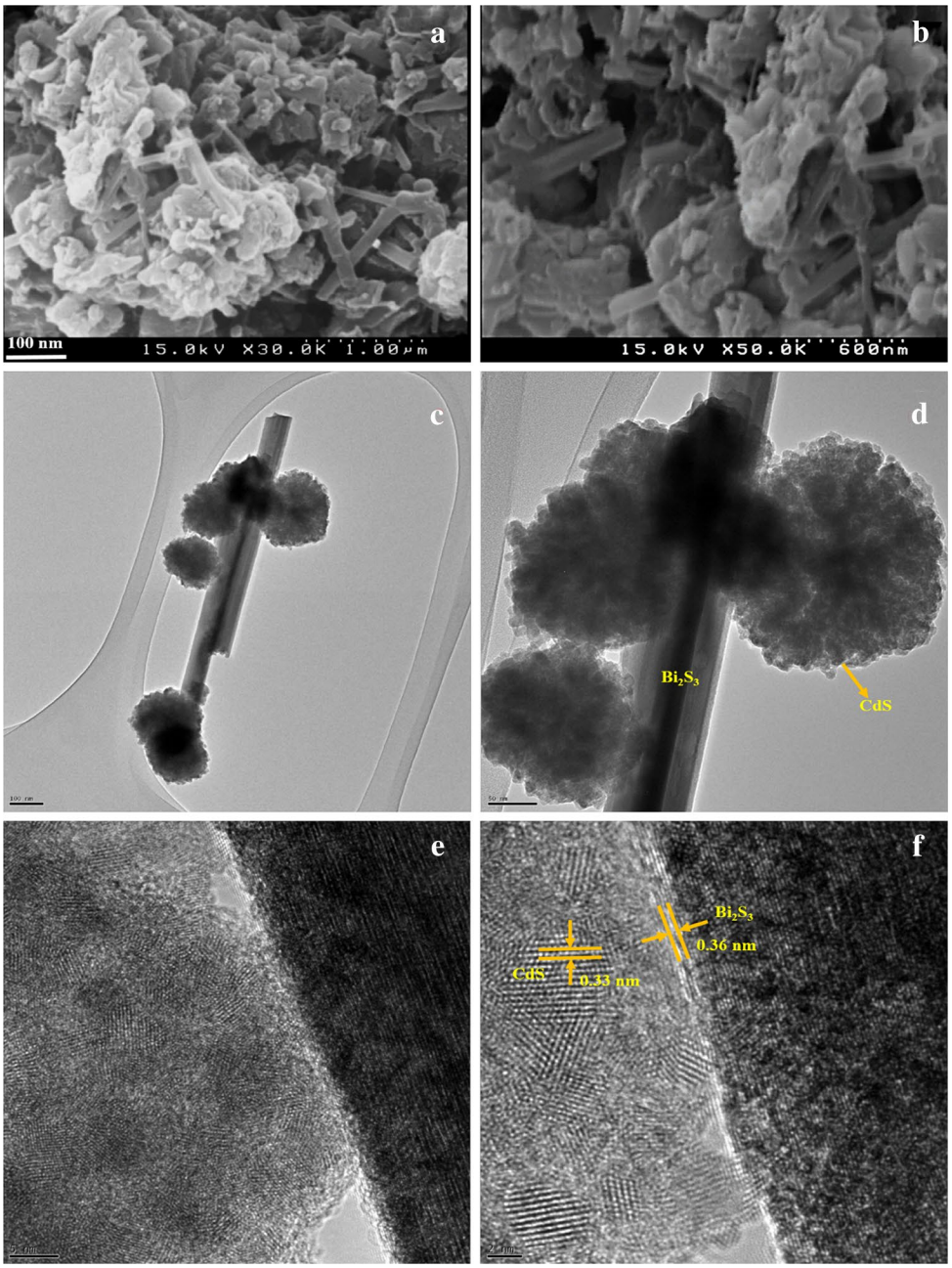

Fig. 2 **a, b** SEM images, **c–f** HRTEM images of CdSQDs/Bi_2S_3 nanocomposite

shows two distinct peaks at 158.51 eV and 163.78 eV. The peaks were assigned to Bi $4f_{7/2}$ and Bi $4f_{5/2}$. In Fig. 4b, the characteristic peaks assigned to the Cd $3d_{5/2}$ and Cd $3d_{3/2}$ binding energies corresponded to 411.97 eV and 404.89 eV, respectively. The difference between the two peaks was 6.69 eV, which represented the abundance of Cd^{2+} on the surface of the photocatalyst [31]. Figure 4c shows two peaks at 161.91 eV and 160.48 eV that represent the S^{2-} ions on the surface of the heterostructure assigned to the $S2p_{1/2}$ and $S2p_{3/2}$ states [31]. A shoulder peak at 161.51 eV in S2p was ascribed to the contribution from the R–S–H groups at the surface of the CdSQDs/Bi_2S_3 nanocomposite, originating from the partial decomposition of the organic groups in the photocatalyst [32]. The XPS results further confirmed the formation of the heterojunction between the CdSQDs and Bi_2S_3.

A N_2 adsorption–desorption (BET) analysis was conducted to verify mesoporous nature of composite. The N_2 adsorption/desorption isotherms and pore size distribution of the Bi_2S_3, CdSQDs, and CdSQDs/Bi_2S_3 nanocomposite are shown in Fig. 5. At a high relative pressure (P/P_0), a diverse hysteresis loop was observed, representing the typical type-IV characteristics of the isotherms. The BET results showed that the specific surface area of this

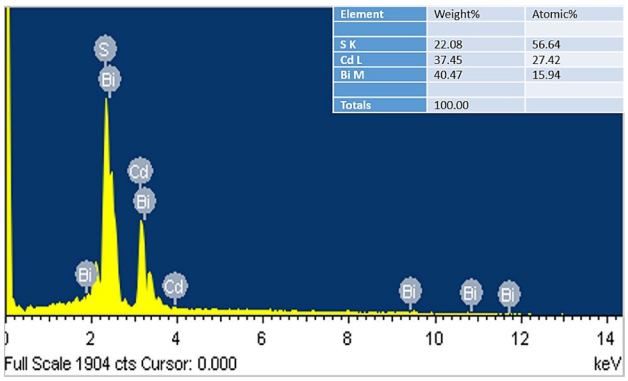

Fig. 3 SEM EDX spectra of CdSQDs/Bi_2S_3 nanocomposite

composite was 33.75 m^2g^{-1}, which is higher than that of pristine Bi_2S_3 as reported in the literature [13, 33]. A higher surface area could provide a larger number of catalytically active sites to improve the simulated solar-driven hydrogen production. Therefore, the large surface area could benefit the photocatalysis process, improving photocatalytic hydrogen production.

Figure 6 shows the FTIR spectra of CdSQDs, Bi_2S_3 and the CdSQDs/Bi_2S_3 nanocomposites. Figure 6a shows the FTIR spectra of CdSQDs. The obvious broad band at around 3347 cm^{-1} is ascribed to the stretching vibration of O–H groups for the CdSQDs. The other reasonable peak originated at 1644 cm^{-1} can be assigned to adsorbed water. The band peaks at 1091 cm^{-1} and 611 cm^{-1} can be ascribed to stretching vibration of absorbed surfactant and C–H stretching modes, respectively [8]. The formation of Bi_2S_3 was confirmed by the vibrational peaks at approximately 535 cm^{-1}, 761 cm^{-1}, and 838 cm^{-1}, which were consistent with the reported literature [34, 35]. However, the CdSQDs/Bi_2S_3 nanocomposites showed functional group peaks at 3431 cm^{-1}, 1605 cm^{-1}, and 1371 cm^{-1} assigned to the distinctive peak of surface OH, adsorbed water bending vibrations (H–O–H), and stretching vibrations of C–O of EG (solvent), respectively (Fig. 6b). The characteristic peaks at 580 cm^{-1} corresponded to the Bi–S or S–Cd bonds present in the heterostructure [24].

The performances of the prepared Bi_2S_3, CdSQDs, and CdSQDs/Bi_2S_3 nanocomposite photocatalysts for H_2 production were examined under simulated sunlight irradiation. The reaction was performed in a Na_2SO_3 and Na_2S

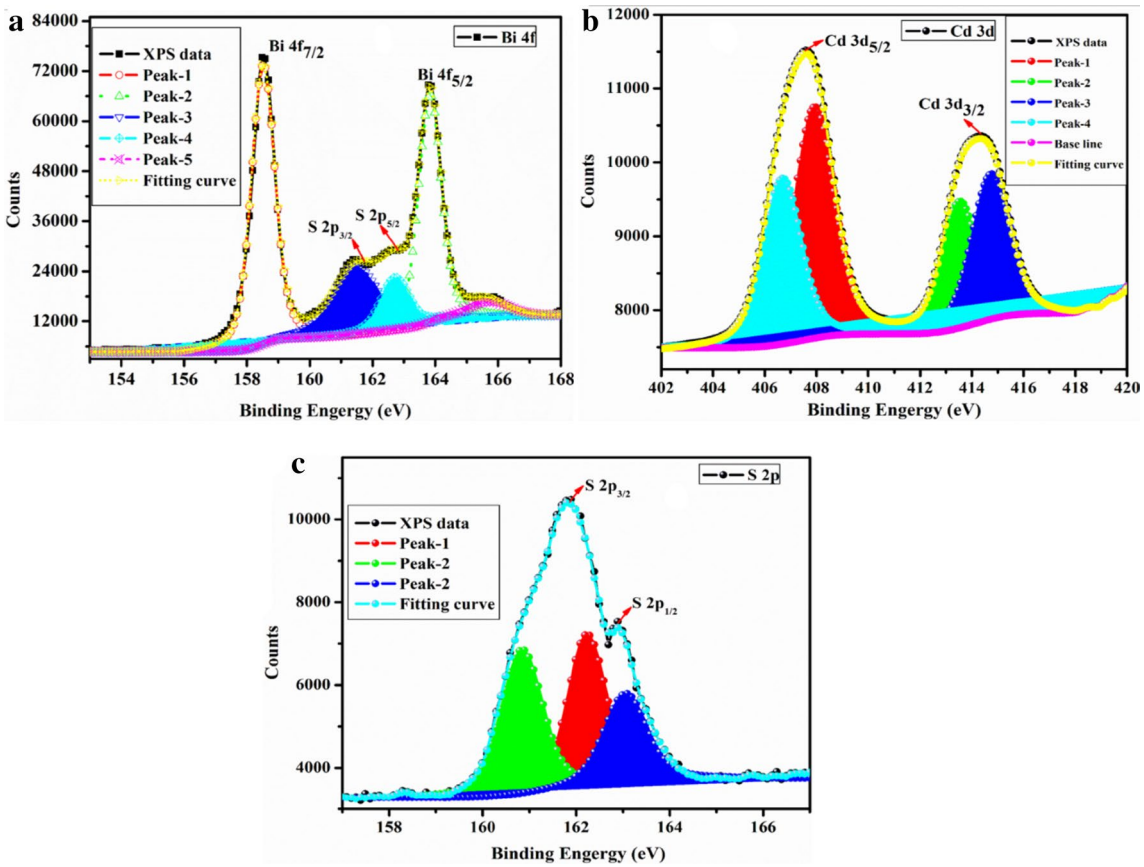

Fig. 4 XPS spectra of **a** Bi 4f; **b** Cd 3d; and **c** S 2p elements of CdSQDs/Bi_2S_3 nanocomposite

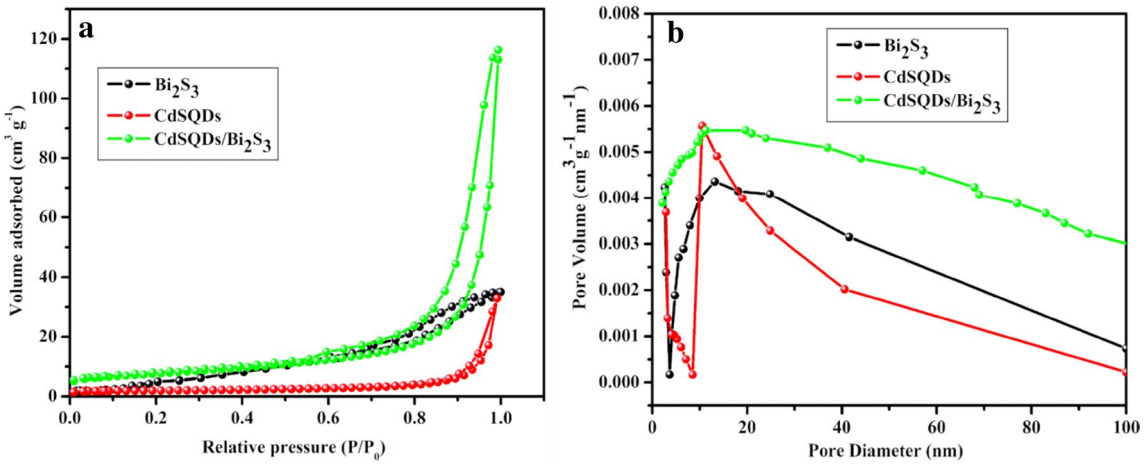

Fig. 5 **a** N_2 adsorption/desorption isotherms and **b** Barrett–Joyner–Halenda (BJH) pore size distribution data of the Bi_2S_3, CdSQDs, and CdSQDs/Bi_2S_3 nanocomposite

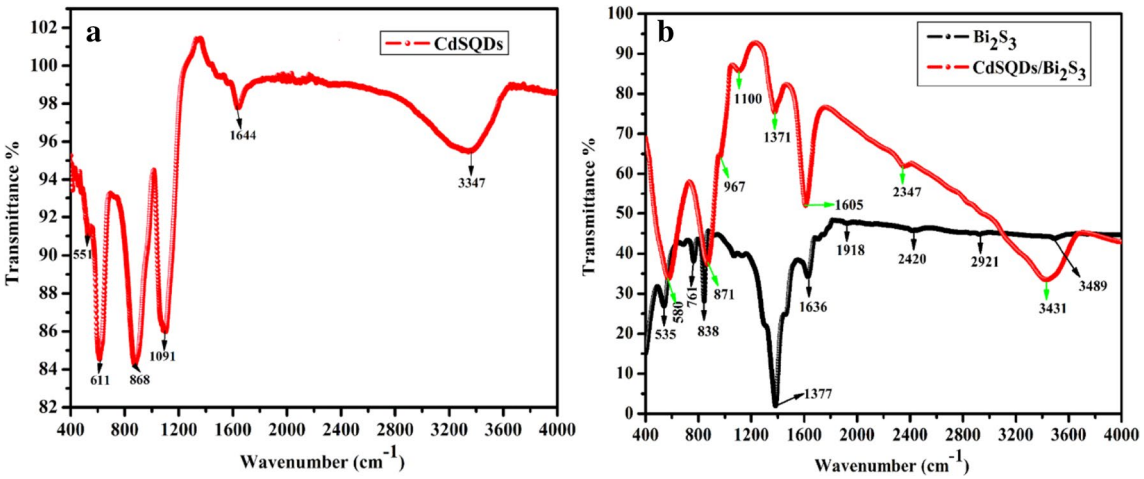

Fig. 6 FTIR spectra of **a** CdSQDs, **b** Bi_2S_3 and CdSQDs/Bi_2S_3 nanocomposite

saturated aqueous solution at ambient conditions. Based on the gas chromatograph, H_2 was detected. As shown in Fig. 7a, the CdSQDs/Bi_2S_3 nanocomposite photocatalysts exhibited improved activity of H_2 production compared with the pure Bi_2S_3 and CdSQDs catalysts. The CdSQDs/Bi_2S_3 nanocomposite photocatalyst demonstrated a higher photocatalytic H_2 production rate (41.67 mmol g^{-1} h^{-1}) than that of the pristine catalysts. Compared with the previously reported catalysts, the CdSQDs/Bi_2S_3 nanocomposite catalysts were capable of H_2 production in an aqueous solution (Table 1), owing to the high H_2 production rate. Among the catalysts in Table 1, the CdSQDs/Bi_2S_3 nanocomposite exhibited an excellent hydrogen production rate owing to the suitable band position of the heterostructure. The hourly progression of the H_2 production test showed that the H_2 yield increased linearly with the reaction time during the 5-h test, as shown in Fig. 7b, representing a linear improvement in the photocatalytic activity with the CdSQDs/Bi_2S_3 nanocomposite catalyst for the durative reaction process. In a previous study, Li et al. [36] reported that a Bi_2S_3 nanorod film demonstrated a photocatalytic hydrogen production of 0.93 µmol in 6 h from an H_2S aqueous solution, which is a lower value than that of the Bi_2S_3 nanorods (2.1 mmol in 5 h) in this study.

Figure 8a shows the migration efficiency and photogenerated charge carrier separation and transport of the Bi_2S_3, CdQDs, and CdSQDs/Bi_2S_3 nanocomposite catalysts using a photocurrent response of a few consecutive on/off lighting cyclic intervals. The Bi_2S_3 and CdSQDs catalysts showed a small photocurrent density (0.02 mA cm^{-2} and 0.025 mA cm^{-2}, respectively) owing to its limited light harvesting capacity. The CdSQDs/Bi_2S_3 nanocomposite catalyst

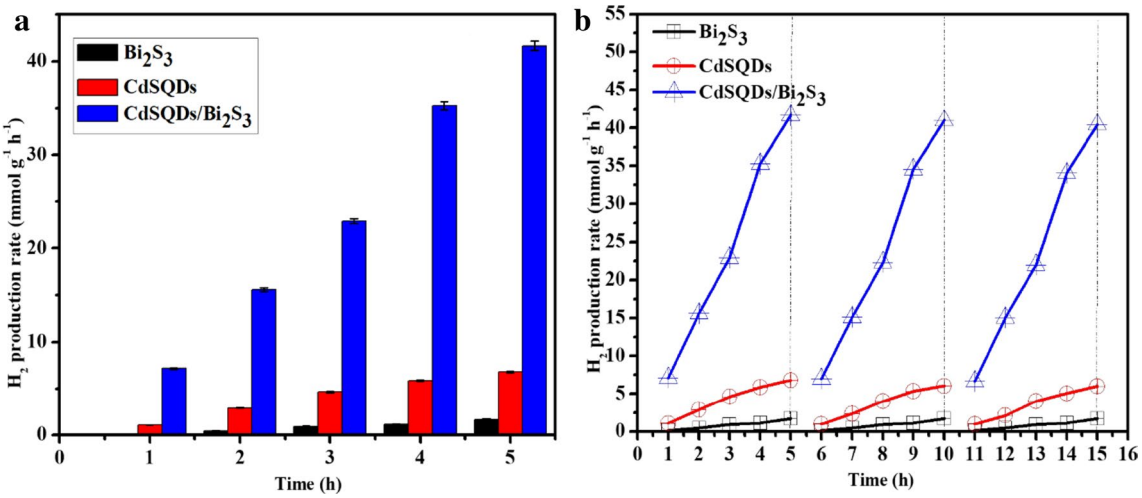

Fig. 7 **a** Photocatalytic H_2 evolution over pristine Bi_2S_3, CdSQDs and CdSQDs/Bi_2S_3 nanocomposite in Na_2SO_3 and Na_2S: water mixtures under simulated solar light irradiation, and **b** experimental results of photocatalytic cycle experiment

Table 1 Comparison of the specific capacitance performance between this study and previous reports on various materials

Name of the photocatalyst	Light details	Scavengers	Hydrogen production rate	References
Bi_2S_3–ZnSe	500W Xenon lamp	NA	2600 μmol g^{-1}	[37]
Bi_2S_3/TiO_2	UV lamp; intensity: 18W cm^{-2}/365 nm	Methanol	14.2 mL	[38]
Bi_2S_3/Y-zeolite	Tungsten lamps 200 W; 29 mW cm^{-2}	1M KOH + 0.1 M $Na_2S_2O_3$	292 μmol g^{-1} h^{-1}	[39]
Bi_2S_3/TiO_2	Tungsten lamps (200 W)	KOH (1 M)	2.9 μmol mg^{-1} h^{-1}	[40]
CdS/Bi_2S_3/FeTCPP	300W Xe lamp, 260 mW cm^{-2}	Acetonitrile/water/TEOA (3:1:1)	6.08 mmol $g^{-1}h^{-1}$	[41]
Bi_2S_3-ZnS	300 W xenon lamp	0.35 M Na_2S and 0.25 M Na_2SO_3	176.24 μmol h^{-1}	[42]
Bi_2S_3 nanowire @ TiO_2 nanorod	150W xenon lamp	0.35 M Na_2SO_3 and 0.25 M Na_2S	35.97 μmol cm^{-2} h^{-1}	[43]
Bi_2S_3@MoS_2	500 W Xe lamp	0.5 M Na_2S and 0.5 M Na_2SO_3	61.4 μmol h^{-1}	[44]
Bi_2S_3/ZnO	Xe-arc lamp (250 W), 100 mW cm^{-2}	Methanol	2791 μmol	[45]
Bi_2S_3/ZrO_2	LED lamps (3 W) of blue light λ = 540 nm	Methanol	1476 μmol $h^{-1}g^{-1}$	[46]
CdSQDs@Bi_2S_3	300 W Xenon lamp (Max 303), 50 mW cm^{-2}	0.25 mol L^{-1} of each Na_2SO_3 and Na_2S	41.67 mmol $g^{-1}h^{-1}$	This work

showed a larger photocurrent density (0.034 mA cm^{-2}) than that of the Bi_2S_3 catalyst, which could be because of the high visible light absorption capacity of the CdSQDs. The photocurrent intensity rapidly decreased when the light source turned it off, indicating that the induced photo electrons transferred to the ITO electrode to produce photocurrents under the simulated solar light. Therefore, coupling of the CdSQDs with the Bi_2S_3 nanorods could increase the hydrogen production rates. In addition, the EIS analysis (Fig. 8b) showed a smaller semicircular area for the CdSQDs/Bi_2S_3 nanocomposite catalyst than that of the Bi_2S_3 and CdSQDs catalyst, proving that the CdSQDs/Bi_2S_3 nanocomposite demonstrated a rapid interfacial photoinduced charge transfer owing to the formation of the heterostructure and sensitization of the CdSQDs. Because of the photoinduced charge carrier separation and transfer, the final contribution in the simulated solar driven photocatalytic hydrogen production comprised the surface catalytic redox reactions initiated by more active sites on the CdSQDs/Bi_2S_3 heterostructure.

Figure 9 shows the plausible photocatalytic mechanism for the simulated solar light driven hydrogen production using the CdSQDs/Bi_2S_3 nanocomposite as a photocatalyst and Na_2SO_3/Na_2S as the electron donors. Under simulated solar light irradiation, the CdSQD and Bi_2S_3 materials absorbed the light owing to their narrow band gap energies.

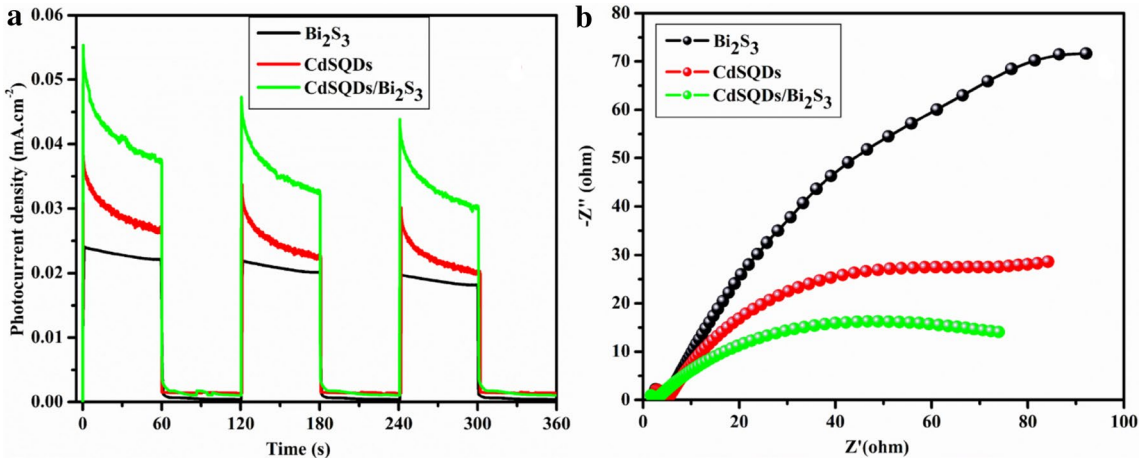

Fig. 8 **a** Photocurrent responses of the PEC cells, and **b** electrochemical impedance spectra over pristine Bi_2S_3, CdSQDs and CdSQDs/Bi_2S_3 as working electrode

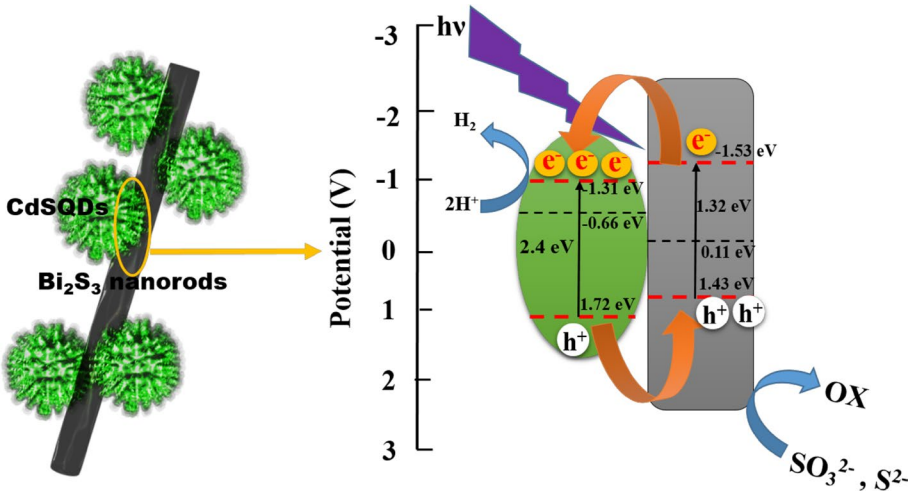

Fig. 9 Plausible photocatalytic mechanism of CdSQDs/Bi_2S_3 nanocomposite

As per the band gaps positions, the band edge position of CB and VB for Bi_2S_3 are 0.11 eV and 1.43 eV, while for CdSQDs are − 0.66 eV and 1.72 eV, respectively. However, under the solar light irradiation, both Bi_2S_3 and CdSQDs can be photoexcited up to higher potential edge positions of − 1.53 eV and − 1.31 eV due to the higher photon energy [47]. Based on the band position of conduction band (CB) and valence band (VB), the photoinduced electrons could reach CdSQDs from the Bi_2S_3 through their phase interface. Therefore, the variance between the transfers rates of the charge carriers created charge carrier separation at their interface, which is beneficial for the associated photo-chemical reactions. The electrons reached CdS faster than the holes, resulting in a high density of holes inside the Bi_2S_3 [47]. The photocatalysts are typically covered by water and sacrificial agent molecules, which can act as electron donors in the photo-chemical reactions. The holes transferred to the surface of the catalyst could react directly with the surface H_2O molecules to produce $OH^{\cdot}$ radicals by the following reactions [48].

$$2H_2O + 2h_{VB}{}^{+} \rightarrow H_2O_2 + 2H^{+} \quad (1)$$

$$H_2O_2 \rightarrow 2OH \quad (2)$$

Thus, the CdSQD@Bi_2S_3 nanocomposite could transfer and separate the electron and holes at their interface under simulated solar light illumination. Based on this mechanism, the superior hydrogen evolution activity could be ascribed to the (i) effective and strong interface between the CdSQD and Bi_2S_3 materials, (ii) high light absorption capability, (iii) large specific surface area, and (iv) suitable band positions of both materials.

In this study, the superior photocatalytic hydrogen production rate of the CdSQDs/Bi_2S_3 nanocomposite was

obtained from the suitable band gap structure, quantum size, dimensionality, and structural features of the nanocomposite [49]. The absence of the CdSQDs at the surface of the Bi_2S_3 nanorods could be ascribed to the insufficient energy or crystal seeds for the formation of the heterostructures [35]. The well crystallized CdSQDs influenced the band gap energies and improved the accessible specific surface area, resulting in improved photocatalytic hydrogen production efficiency.

4 Conclusions

CdSQDs/Bi_2S_3 heterojunction photocatalysts were synthesized using a simple chemical mixing method. EG could inhibit the appearance of the impure crystal phase for the synthesis of CdSQD nanobunches to couple them with Bi_2S_3 nanorods, creating a heterojunction, which benefited the photocatalytic hydrogen evolution. The prepared CdSQDs/Bi_2S_3 heterojunction controlled the capacity to utilize efficient solar light and create a moderate morphology. Consequently, the photocatalytic hydrogen production rate was 41.67 mmol g^{-1} h^{-1}, which is 24.9-fold higher than that of pristine Bi_2S_3. The electrochemical studies revealed effective charge carrier separation and transfer at the CdSQDs/Bi_2S_3 heterojunction interface owing to adequate contact.

Acknowledgements This work was supported by the National Research Foundation of Korea (NRF) and funded by the Ministry of Science, ICT, and Future Planning (2017R1A2B1004860) and 2017R1A4A1015581.

References

1. W. Shangguan, A. Yoshida, J. Phys. Chem. B **106**(47), 12227–12230 (2002)
2. J.L. Borges, F.L.P. Pessoa, E.M. Queiroz, Ind. Eng. Chem. Res. **51**(39), 12877–12885 (2012)
3. S.Z. Baykara, Int. J. Hydrogen Energy **43**(23), 10605–10614 (2018)
4. F. Rahmawati, L. Yuliati, I.S. Alaih, F.R. Putri, J. Environ. Chem. Eng. **5**(3), 2251–2258 (2017)
5. X. Gan, D. Lei, K. Wong, Mater. Today Energy **10**, 352–367 (2018)
6. Q. Li, B. Guo, J. Yu, J. Ran, B. Zhang, H. Yan, J. Ru Gong, J. Am. Chem. Soc. **133**(28), 10878–10884 (2011)
7. J. Li, J. Lin, Mater. Lett. **221**, 289–292 (2018)
8. Y. Liu, F. Gao, L. Wang, W. Yang, X. He, H. Hou, J. Mater. Sci.: Mater. Electron. (**in press**)
9. L. Cheng, Q. Xiang, Y. Liao, H. Zhang, Energy Environ. Sci. **11**, 1362–1391 (2018)
10. R. Dang, X. Ma, J. Mater. Sci.: Mater. Electron. **28**(12), 8818–8823 (2017)
11. J. Li, X. Qian, Y. Peng, J. Lin, Mater. Lett. **224**, 82–85 (2018)
12. F. Cheng, H. Yin, Q. Xiang, Appl. Surf. Sci. B, **391**, 432–439 (2017)
13. S.V.P. Vattikuti, A.K.R. Police, J. Shim, C. Byon, Sci Rep. **8**, 4194 (2018)
14. L. Yan, Y. Wang, H. Shen, Y. Zhang, J. Li, D. Wang, Appl. Surf. Sci. **393**, 496–503 (2017)
15. Y. Mi, H. Li, Y. Zhang, R. Zhang, W. Hou, Appl. Surf. Sci. **423**, 1062–1071 (2017)
16. H. Shi, Y. Zhaoa, J. Fan, Z. Tang, Appl. Surf. Sci. **465**, 212–222 (2019)
17. Q. Zhang, Z. Dai, G. Cheng, Y. Liu, R. Chen, Ceram. Int. **43**, 11296–11304 (2017)
18. S. Vadivel, V.P. Kamalakannan, N. Keerthi, Balasubramanian, Ceram. Int. **40**, 14051–14060 (2014)
19. G. D.Xiong.Huang, B.Zhou, Q., A. Yan, W. Pan, Huang, J. Colloid Interface Sci. **464**, 103–109 (2016)
20. F. Chen, Y. Cao, D. Jia, J. Colloid Interface Sci. **404**, 110–116 (2013)
21. W. Wang, H. Cheng, B. Huang, X. Lin, X. Qin, X. Zhang, Y. Dai, J. Colloid Interface Sci. **402**, 34–39 (2013)
22. A. Chachvalvutikul, W. Pudkon, T. Luangwant, T. Thongtem, S. Thongtem, S. Kittiwachan, S. Kaowphong, Mater. Res. Bull. **111**, 53–60 (2019)
23. C. Li, W. Chen, J. Yuan, M. Chen, W. Shangguan, World J. Nano Sci. Eng. **1**, 79–83 (2011)
24. L. Hao, G. Chen, Y. Yu, Y. Zhou, Z. Han, Y. Liu, Int. J. Hydrogen Energy **39**, 14479–14486 (2014)
25. X. Li, J. Chen, H. Li, J. Li, Y. Xu, Y. Liu, Ji. Zhou, J. Nat. Gas Chem. **20**(4), 413–417 (2011)
26. S.V.P. Vattikuti, J. Shim, C. Byon, J. Mater. Sci.: Mater. Electron. **28**, 14282–14292 (2017)
27. M. Shakouri-Arania, M. Salavati-Niasar, New J. Chem. **38**, 1179–1185 (2014)
28. H. Park, Y.K. Kim, W. Choi, J. Phys. Chem. C **115**, 614 (2011)
29. R. Hamood, M.S.A. El-sadeb, A. Gadalla, Vacuum **157**, 291–298 (2018)
30. B. Bajorowicz, E. Kowalska, J. Nadolna, Z. Wei, M. Endo, B. Ohtani, A. Zaleska-Medynska, Dalton Trans. **47**, 15232–15245 (2018)
31. J. Kavil, A. Alshahrie, P. Periyat, Nano-Struct. Nano-Object. **16**, 24–30 (2018)
32. M. Fantauzzi, B. Elsener, D. Atzei, A. Rigoldi, A. Rossi, Exploiting xps for the identification of sulfides and polysulfides. RSC Adv. **5**, 75953–75963 (2015)
33. K. Liang, C. Wang, X. Xu, J. Leng, H. Ma, Phys. Lett. A **381**(6), 652–657 (2017)
34. D. Zhao, W. Wang, W. Zong, S. Xiong, Q. Zhang, F. Ji, X. Xu, Mat. **10**(8), 891 (2017)
35. T.K. Patil, M.I. Talele, J. Nano Electron. Phys. **4**, 040031–040036 (2012)
36. Z. Li, Q. Zhang, M. Dan, Z. Guo, Y. Zhou, Mater. Lett. **201**, 112–118 (2017)
37. I.A. Mkhalid, Ceram. Int. **44**, 22198–22204 (2018)
38. J. Kim, M. Kang, Int. J. Hydrogen Energy **37**, 8249–8256 (2012)
39. A. Abdi, A. Denoyelle, N. Commenges-Bernole, M. Trari, Int. J. Hydrogen Energy **38**, 2070–2078 (2013)
40. R. Brahimi, Y. Bessekhouad, A. Bouguelia, M. Trari, Catal. Today **122**, 62–65 (2007)
41. P. Li, X. Zhang, C. Hou, Y. Chen, T. He, Appl. Catal. B **238**, 656–663 (2018)
42. M. Nawaz, J. Photochem. Photobiol. A **332**, 326–330 (2017)
43. C. Liu, Y. Yang, W. Li, J. Li, Y. Li, Q. Chen, Chem. Eng. J. **302**, 717–724 (2016)
44. W.P. C.Lee, M. Gui, L. Tan, T.Y. Wu, S. Sumathi, S. Chai, Catal. Commun. **98**, 66–70 (2017)

45. S. Bera, S. Ghosh, R.N. Basu, New J. Chem. **42**, 541–554 (2018)
46. C. García-Mendoza, S. Oros-Ruiz, S. Ramírez-Rave, G. Morales-Mendoza, R. López, R. Gómez, J. Chem. Technol. Biotechnol. **92**, 1503–1510 (2017)
47. R.P. Panmand, Y.A. Sethi, R.S. Deokar, D.J. Late, H.M. Gholap, J. Baeg, B.B. Kale, RSC Adv. **6**, 23508–23517 (2016)
48. Z. Fang, Y. Liu, Y. Fan, Y. Ni, X. Wei, K. Tang, J. Shen, Y. Chen, J. Phys. Chem. C **115**, 13968–13976 (2011)
49. Z.G. Yi, J.H. Ye, Appl. Phys. Lett. **91**, 254108 (2007)